Self-decorated Au nanoparticles on antireflective Si pyramids with improved hydrophobicity

C. P. Saini, A. Barman, M. Kumar, B. Satpati, T. Som, and A. Kanjilal'

Citation: Journal of Applied Physics **119**, 134904 (2016); doi: 10.1063/1.4945379
View online: http://dx.doi.org/10.1063/1.4945379
View Table of Contents: http://aip.scitation.org/toc/jap/119/13
Published by the American Institute of Physics

Self-decorated Au nanoparticles on antireflective Si pyramids with improved hydrophobicity

C. P. Saini,[1] A. Barman,[1] M. Kumar,[2] B. Satpati,[3] T. Som,[2] and A. Kanjilal[1,a)]
[1]*Department of Physics, School of Natural Sciences, Shiv Nadar University, Gautam Buddha Nagar, Uttar Pradesh 201 314, India*
[2]*SUNAG Laboratory, Institute of Physics, Bhubaneswar 751 005, Odisha, India*
[3]*Surface Physics and Material Science Division, Saha Institute of Nuclear Physics, Kolkata 700 064, India*

(Received 6 December 2015; accepted 23 March 2016; published online 5 April 2016)

Post-deposition annealing mediated evolution of self-decorated Au nanoparticles (NPs) on chemically etched Si pyramids is presented. A distinct transformation of Si surfaces from hydrophilic to hydrophobic is initially found after chemical texturing, showing an increase in contact angle (CA) from 58° to 98° (±1°). Further improvement of hydrophobicity with CA up to ∼118° has been established after annealing a 10 nm thick Au-coated Si pyramids at 400 °C that led to the formation of Au NPs on Si facets along with self-ordering at the pyramid edges. Detailed x-ray diffraction studies suggest the evolution of crystalline Au NPs on strained Si facets. Microstructural studies, however, indicate no mixing of Au and Si atoms at the Au/Si interfaces, instead of forming Au nanocrystals at 400 °C. The improved hydrophobicity of Si pyramids, even with Au NPs can be explained in the light of a decrease in solid fractional surface area according to Wenzel's model. Moreover, a sharp drop in specular reflectance from Si pyramids in the range of 300–800 nm, especially in the ultraviolet region up to ∼0.4% is recorded in the presence of Au NPs by ultraviolet-visible spectroscopy, reflecting the possible use in photovoltaic devices with improved antireflection property. © *2016 AIP Publishing LLC*. [http://dx.doi.org/10.1063/1.4945379]

I. INTRODUCTION

Artificially designed hydrophobic surfaces exhibiting self-cleaning property have attracted a considerable attention due to their potential to be used in various applications such as biomedical drug delivery, impermeable textiles, sensors, anti-icing, and solar panels (Ref. 1 and references therein). The hydrophobic state with contact angle (CA) > 90° (Ref. 2) has commonly been discussed in terms of Wenzel and/or Cassie-Baxter models,[3] where both of them rely on the aspect ratio and spatial distribution of low dimensional structures, and so the solid fractional surface area.[4] The Wenzel's model is basically associated with the penetration of water droplets into the grooves of a rough surface for complete wetting, while water droplet in the case of Cassie-state sits onto the solid-air composite surface without wetting the valley region.[5] Nevertheless, the transition from Wenzel to Cassie-Baxter state is also driven by surface chemical property.[2,6] Moreover, inspired by the self-cleaning ability of a lotus leaf with micro/nano dual-scale roughness,[7] easy and large-scale fabrication of such smart structures have now become a frontier field of research. In order to fulfill this, the artificial structures have recently been prepared by several methods that include lithographic patterning,[8] vapor-liquid-solid method,[9] chemical route on self-assembled textures,[10] as well as an inexpensive chemical etching process.[5,11] The last approach is advantageous for Si due to its large scale application in semiconductor industries, especially in crystalline Si solar cells with improved antireflection (AR) property in the presence of surface pyramids.[12] However, in order to enhance hydrophobic behavior and for preventing the surface from being contaminated, chemically etched Si pyramids are required to manipulate further for reducing the fractional surface area by modifying the faceted surface using suitable nanostructures.[11,13]

Among several ways of producing nanostructures,[2,5] the formation of dual-scale roughness by utilizing metal nanoparticles (NPs) or nanocomposites has attracted further interest for improving the hydrophobic behavior.[14] Au NPs are important in this respect due to their intrinsic hydrophobic nature (as the one observed on sputter deposited nanostructured surfaces)[15] and chemical stability,[16] besides their common use as functionalized NPs,[17] catalyst,[11] or as mask for developing dual-scale Si structures.[18] It is therefore not only imperative to explore the growth of Au NPs on Si pyramids for finding suitable structures towards improving hydrophobicity but also important to understand the mechanism involved under hostile environments, especially for solar cells.[19] In order to fabricate Au NPs, solid state dewetting is one of the most common and cost effective approaches in which edge agglomeration started via capillary edge instability through minimizing surface free energy below the melting point followed by the formation of NPs due to Rayleigh instability.[20]

The ability of Au NPs in light coupling with the substrate underneath, especially for Si will be beneficial too for advancing the performance of a solar absorber.[21] The light trapping phenomenon can further be enhanced by introducing ordered NPs,[22] which are often prepared by various approaches such as lithographic technique,[23] solid state dewetting,[24] porous templates,[25] and scanning probe techniques.[26] However, large scale production of self-ordered Au NPs within a moderate

a)Electronic mail: aloke.kanjilal@snu.edu.in

cost is not only challenging but also interesting from fundamental standpoint.

This article reports a simple approach to produce Au NPs on chemically textured Si surfaces consisting of a self-ordered structure at the pyramid edges. In particular, it is shown how conformal Au layer on strained Si pyramid surfaces can facilitate formation of self-decorated Au NPs on Si pyramids by annealing at 400 °C. Moreover, it has further been shown that Si with native oxide becomes hydrophobic after surface texturing with a CA of ~98°, though it increases further up to ~118° in the presence of Au NPs. It is also shown how the Si pyramids can suppress the specular reflectance, especially in the presence of Au NPs in ultraviolet (UV) range.

II. EXPERIMENTAL

A 500 μm thick *p*-type Si(100) wafer was diced into pieces with an average area of $1 \times 1\,cm^2$. Ultrasonically cleaned Si wafers were initially cleaned with saw-damage-removal (SDR) approach, where Si substrates were immersed into a 30 wt. % NaOH solution (in H_2O) at 75 °C for 3 min during which both top and rear surfaces were cleaned by removal of 5–7 μm thick Si from either surface. Afterwards, controlled chemical texturing was executed at 70 °C for 40 min in 3 wt. % NaOH solution in the presence of 10% isopropyl-alcohol (IPA); details can be found in Ref. 12. Following this, about 10 ± 1 nm thick Au film was deposited at room temperature (RT) on textured Si (after removing native oxide in 5% HF solution) by electron-beam deposition technique. The pressure inside the chamber was $\sim 2 \times 10^{-6}$ mbar during Au deposition, while the source-to-substrate distance was ~13 cm. A 160 W DC power was supplied to the substrate rotating with a speed of 18 rpm for achieving uniform film thickness. The Au films were then annealed at 300 °C and 400 °C in vacuum with a base pressure of $\sim 1 \times 10^{-3}$ mbar for an hour separately in a split furnace (MTI, OTF-1200X) to follow the temperature dependent formation of Au NPs below and above the eutectic point of Au on Si substrate (~359 °C).[27]

Surface morphology of Au films on both flat and textured Si was studied by field-emission scanning electron microscopy, SEM (Carl Zeiss) before and after annealing, while fine details were characterized by atomic force microscopy, AFM (Park, XE-007). The thickness of as-deposited Au films was measured on flat Si by stylus profilometer with a resolution of 0.5 nm (Bruker, DektakXT). Moreover, crystalline phases were identified by x-ray diffraction, XRD (Bruker, D8-Discover) using a Cu-K_α radiation ($\lambda = 0.154$ nm). Microstructures were examined by transmission electron microscopy (TEM) operating at 300 keV (FEI Tecnai G^2 S-Twin) in cross-sectional geometry, while elemental profile was studied by energy dispersive x-ray spectroscopy (EDS). Cross-sectional TEM (XTEM) specimens were prepared using the standard method of mechanical polishing and dimpling with final thinning using a precision-ion-polishing system (PIPS, Gatan, Pleasanton, CA). The ion beam polishing was carried out with 3 keV Ar^+-ions without liquid nitrogen cooling followed by 1.2 keV cleaning process. For TEM investigations, specimens were aligned along the [110] zone axis and cooled down to liquid nitrogen temperature to avoid possible electron induced structural modification. Electron energy loss spectroscopy (EELS) has also been employed for further understanding.

The hydrophobic property of Si facets with and without Au NPs was investigated by CA measurements (Data Physics, OCA 15Pro system) with software-controlled pendant drop mode, where 2 μl droplets of deionized water were dropping on the sample surfaces. To confirm the recorded CAs, similar experiments were again performed in another CA system (Krüss GmbH, DSA-25). In any case, a CCD camera equipped with a magnifying lens was used for capturing the droplet images and confirms the repeatability of the recorded data at different positions on each sample. The errors in the measured CAs are found to be within ±1°. In addition, specular reflectance was examined by UV-visible (UV-VIS) spectrophotometer (Shimadzu, 3101PC) in the wavelength range of 300–800 nm with unpolarized light, where the incident light was falling on the target at an angle of 45° with respect to surface normal.

III. RESULTS AND DISCUSSION

The SEM image in Fig. 1(a) displays the formation of Au NPs on a flat Si surface at 400 °C (called Au 400 °C/Si_{Flat}), while their size distribution depicts a bell-shape feature with a maximum at ~100 nm (inset), in good agreement with the previous report.[28] On the other hand, SEM image shown in Fig. 1(b) exhibits the conformal growth of an Au layer at RT on the {111} facets of Si pyramids with an average rms roughness of ~1.7 nm as revealed from AFM, while it is of ~3 nm at the apex [indicated by dashed square in the inset of Fig. 1(b)]. When annealed at 300 °C, an evolution of Au NPs on microscale Si pyramids was observed in cross-sectional geometry by tilting the sample at 10° from the surface normal [Fig. 1(c)], while a typical distribution of Au NPs was established by plan-view SEM (inset). Temperature-induced formation of Au NPs can be explained in the light of dewetting of thin Au layer, where the competition between thermodynamics (that drives a system towards low surface energy) and kinetics (that prevents the system to go for low surface energy) of Au atoms dictate the structural evolution.[29] Since the Au film was deposited at RT, the adatoms cannot move significant distances due to the lack of sufficient kinetic energy by overcoming the surface energy barrier, and eventually form a continuous metastable film. With increasing annealing temperature, thermodynamics however will drive the system towards the equilibrium state via atomic diffusion that leads to the formation of nanostructures for achieving minimum surface free energy.[29] *However, the key finding is the formation of Au NPs on Si facets in conjunction with self-ordering along the pyramid edges at* 400 °C [marked by dashed rectangle and circle in Fig. 1(d)]. The magnified SEM image after annealing at 400 °C (Au 400 °C/Si_{Tex}) is displaying in the inset of Fig. 1(d) reflecting the self-ordered Au NPs at the edges of a Si pyramid. In any case, the formation of Au NPs can be argued again on the ground of solid-state dewetting[29] of the conformal Au layer, though the formation of self-ordered Au NPs is most likely driven by the defects residing at the intersection of the adjacent {111} Si facets.[24] In fact, higher diffusion rate of Au near the pyramid edges

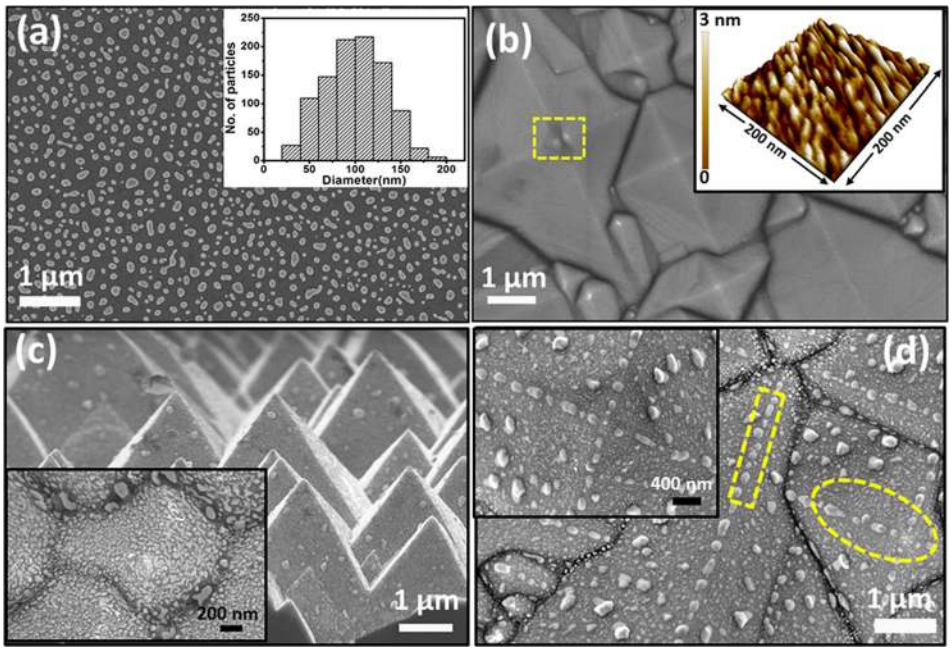

FIG. 1. Plan-view SEM image showing (a) Au NPs on flat Si annealed at 400 °C, while inset represents the corresponding particle size distribution. (b) Conformal growth of Au film on Si facets at RT, while the AFM image (inset) gives the magnified view of the pyramid apex (marked by rectangular dashed box). (c) Cross-sectional SEM image after annealing at 300 °C, while the plan view micrograph (lower inset) indicates the formation of Au NPs. (d) Self-ordered Au NPs at 400 °C along the pyramid edges (marked by dashed rectangular box and circle), also prominent in the magnified image (inset).

can favor the development of nucleation sites[30] near the vicinity of defects. Among various models, recent theoretical understanding suggests that the change in solid state epitaxial recrystallization rate on the {111} twin surfaces plays an important role behind defect formation.[31]

Besides dewetting, negative chemical potential at the pyramid edges with lower coordination of atoms may also play a decisive role in self-diffusion of Au atoms[24,29] followed by the growth of one-dimensional NPs. The later one can be understood in the light of Gibbs-Thomson relation:[24] $\Delta\mu = \kappa\ \gamma\ \Omega$, where $\Delta\mu$ represents local excess chemical potential, κ is the local curvature, γ is the surface energy, and Ω is the atomic volume. On the other side, positive chemical potential in the pyramid apex can also give rise to an out-diffusion of Au atoms, which eventually do not allow forming Au NP, in consistent with the SEM results [see Fig. 1(d)]. Moreover, it seems that Au atoms far from the pyramidal edges are not participating in forming self-ordered Au NPs, rather they form bigger islands by agglomerating locally via the Ostwald ripening mechanism.[32]

To understand the impact of aperiodicity and imperfectness of Si pyramids (for having protrusions jutting out from the {111} facets[12]), structural analysis has initially been performed by XRD.[33] Here, the structures of pristine Si (Si_{Flat}) and chemically textured Si (Si_{Tex}) were systematically investigated using coupled $\theta - 2\theta$ mode for 2θ in the range of 30°–75° [see Fig. 2(a)], where θ is the Bragg's angle. As can be seen from Fig. 2(a), dominant peaks located at ~32.98° and 69.15° in Si_{Flat} can be attributed to reflections from the (200) and (400) planes, respectively.[12] However, a clear shift in (400) peak position (marked by double arrow) by 0.2° has been recorded after chemical texturing towards higher 2θ value, though a relatively weak peak is also visible at ~69.15° as in Si_{Flat}. The change in peak position can be attributed to the evolution of a *tensile strain*[34,35] in the atomic planes of surface pyramids, whereas the weak peak is likely to be originated from the underneath bulk. The strain in Si_{Tex} is calculated to be of ~0.27% using the formula[34] $(d_s - d_0)/d_0 \times 100\%$, where d_s and d_0 correspond to the inter-planar spacing in the strained and strain-free layers. Consistent with the (400) peak shifting, close inspection (inset, high-resolution XRD with a step of 0.001°) reveals a subtle peak shift of the (200) reflection by 0.1° towards higher 2θ in Si_{Tex}. This is further associated with the increase in full-width at half-maximum (FWHM) and change in peak shape. These results can be attributed to the plastic deformation of atoms on Si facets through spreading of lattice parameters around the average value, while the imperfection along the crystallographic direction of Si facets may be responsible for increasing peak intensity.[36]

Following deposition of Au films, annealing temperature dependent structural modification on both Si_{Flat} and Si_{Tex} surfaces was monitored by Glancing-incidence XRD (GXRD) for 2θ in the range of 35°–70° [Fig. 2(b)] with an incidence angle of 0.5°. The peaks appearing at $2\theta \sim 38.3°$, 44.5°, and 64.7° can be assigned to the reflections from the (111), (200), and (220) planes of Au, respectively,[37] in the absence of any gold-silicide phase up to 400 °C (further

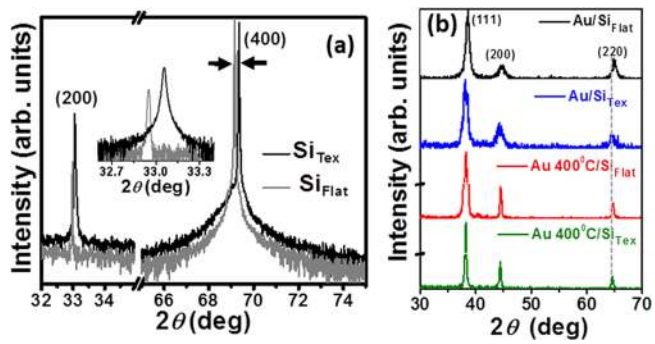

FIG. 2. The XRD patterns of (a) textured (black curve) and flat (grey curve) Si surfaces; inset shows a high resolution XRD near the (200) peak, for clarity. (b) The GXRD patterns of RT grown Au film on flat Si (black) and textured Si (blue), whereas 400 °C annealed Au film on flat Si (red) and textured Si (olive), respectively. Vertical dashed-line indicates position of the (220) reflection.

confirmed by TEM studies as will be discussed in the following). Prior to annealing, polycrystalline peaks are weak and broadened with the FWHM in the order of ~0.59° and 0.39° for 10 nm thick Au layers on both Si_{Flat} and Si_{Tex} surfaces (black and blue curves), though a prominent peak shift of ~0.3° towards higher 2θ is noticed in the former case, revealing the presence of a tensile strain. This phenomenon can be attributed to limited flexibility of Au atoms to follow the cubic lattice structure of pristine Si.[30] However, the plastic deformation in the {111} surfaces of Si pyramids (discussed above) is expected to provide a suitable platform for conformal deposition of the Au layers[30] at RT. The increase in peak intensity with decreasing FWHM up to ~0.24° at 400 °C for both Au 400 °C/Si_{Flat} and Au 400 °C/Si_{Tex} (red and olive XRD patterns) is associated with the formation of Au nanocrystallites [see Figs. 1(a) and 1(d)] with increasing crystalline planes for x-ray reflection. Using the (111) reflection for Au 400 °C/Si_{Tex}, the average size of crystallites is determined to be about 40 ± 3 nm by Scherrer formula:[12] $D = 0.94\lambda/(\beta \cos\theta)$, where D is the average crystal size, β is FWHM, and λ is the wavelength of the incident x-rays. This is also corroborated with the corresponding SEM micrographs (Fig. 1).

For further understanding of the structural properties, especially the role of annealing temperature in the formation of Au NPs on Si pyramids, detailed microstructural analyses were carried out by TEM. Typical XTEM image of the 400 °C/Si_{Tex} sample in bright-field mode is displayed in Fig. 3(a), showing the distribution of Au NPs on Si facets. The high-resolution TEM (HRTEM) images of sections (1) and (2) in the apex and valley regions of a Si pyramid [shown in Fig. 3(a)] are exhibited in Figs. 3(b) and 3(c), respectively. As evidenced, different sizes of spherical Au NPs are formed, though magnified view of the regions [as indicated by downward arrows in Figs. 3(b) and 3(c)] indicates the wetting behavior of Au NPs [highlighted by a dashed elliptical curve in Fig. 3(d)] below the spherical ones on reconstructed Au/Si interface with orientation along {111}, in consistent with the results given in Refs. 38 and 39. This is further evidenced in other pyramids as the one documented in Fig. 3(e), where close examination of the cluster encircled by a dashed circle elucidates the *frozen* intermediate state of coalescence between the adjacent (molten) Au clusters via the Ostwald ripening mechanism.[32] Crystalline Au NPs have also been revealed by further magnification in HRTEM mode [see Fig. 3(f)], showing the evolution of Moiré fringes which can be formed due to small

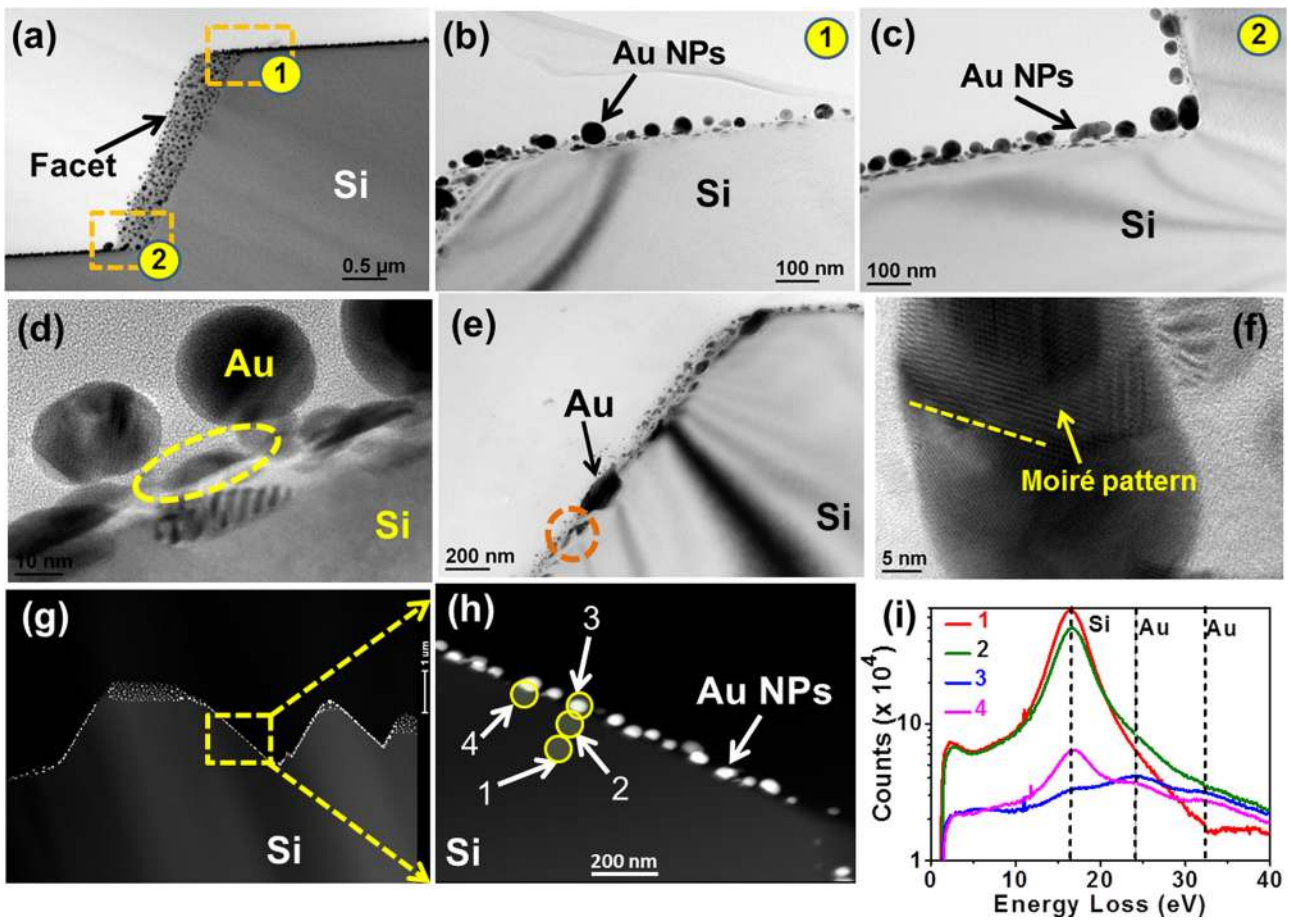

FIG. 3. (a) Bright-field XTEM images show the formation of Au NPs on one of the Si pyramids, where regions (1) and (2) are displayed in (b) and (c), respectively. (d) HRTEM image showing coexistence of both spherical and elongated Au NPs (marked by dashed elliptical curve). This is prominent in (e) indicating incomplete Au clustering (shown by downward arrow) via coalescence of small NPs (indicated by dashed circle). (f) Crystalline feature including Moiré pattern. (g) Low magnification HAADF-STEM image, where the magnified one from the yellow dashed rectangular region is depicted in (h), displaying an array of Au NPs at the Si pyramid edges. (i) The EELS spectra recorded from regions "1" to "4" in (h), showing the plasmon peaks of Si (~16.8 eV), and Au (~24.4 and 33 eV).

deviation of the overlapped planes in the presence of slight rotation and/or curved surfaces.[40] In fact, misfit between the adjacent crystalline planes in Au cluster may be accommodated by introducing a *twin-structure* along the dashed-line without posing Au-Si mixing and in turn can contribute in developing strain in Au nanocrystals, in accordance with GXRD results [Fig. 2(b)]. Since for any given atom, the intensity in high-angle annular dark-field (HAADF) image depends on the atomic number (Z) roughly by $Z^{1.7}$ [Ref. 41], the ratio of Z values of the constituent elements will give the contrast difference in it. Based on this concept, the contrast of Au should be about 18.9 times stronger than that of Si, and thus one can expect a bright contrast from Au NPs with respect to Si, as revealed in Fig. 3(g). The distribution of Au and Si across the Au/Si interfaces is also verified by EDS mapping from Au-*M* and Si-*K* edges (not shown), though it is impossible to follow the atomic mixing at the Au/Si interface.

As the EELS is known to be a sensitive technique for surface/interface analysis, this has been employed for point analysis in close vicinity of the Au/Si interface with an electron beam spot size of ~1 nm. In order to conduct this experiment, initially magnified HAADF image was taken [see Fig. 3(h)] from the yellow dashed box in Fig. 3(g). The low-loss EELS spectra recorded at four different regions [i.e., "1"–"4" in Fig. 3(h)] for an energy window of 1–40 eV [Fig. 3(i)]. A sharp dominant peak appeared at ~16.8 eV (red curve) is attributed to the plasmon signal from the pure Si substrate[42] as indicated by "1" in Fig. 3(h). However, the Si peak intensity is slightly reduced by introducing a broad hump around ~24.4 eV when moved towards the Au/Si interface (spectrum in green for "2"). Detailed analyses suggest that the peak originating at ~24.4 eV is the signature of plasmon from the adjacent Au NP.[40] In this way, the EELS spectrum recorded from the center of Au NPs (blue curve from "3") manifests the dominant behavior of plasmon peaks of Au NPs at ~24.4 eV and ~33 eV.[43] When the EELS spectrum is acquired from the Au/Si interface [indicated by "4" in Fig. 4(h)], the Si plasmon peak intensity together with peaks associated with Au NP is found to be reduced considerably (magenta curve) with respect to the one recorded from "1." This study further reveals that no detectable mixing of Au and Si atoms exists at the Au/Si interface even at 400 °C.

To understand the significance of surface texturing, especially the role of Au NPs on Si micro-pyramids in improving hydrophobicity, CA measurements were carried out systematically for 2 μl water droplet. Initial experiments on Si_{Flat} [schematically shown in Fig. 4(a)] give an average CA of 58° ± 1° (right panel). Although hydrogen-passivated Si surfaces are known to be hydrophobic in nature, the native oxides at surfaces however make them hydrophilic.[44] On the other hand, the anisotropic chemical etching-mediated Si pyramids[12] enhances the surface roughness [see Fig. 4(b)] and in turn offers an average CA of 98° ± 1° (right panel). Moreover, Fig. 4(c) elucidates a clear transformation from hydrophilic-to-hydrophobic surfaces by depositing Au layers on Si_{Flat}, showing a drastic increase in CA from 58° ± 1° to 89° ± 1° (right panel). This can be attributed to the chemical inertness of Au atoms in the presence of low surface energy.[16] However, the CA remains almost unaffected (96° ± 1°) by conformal Au deposition on

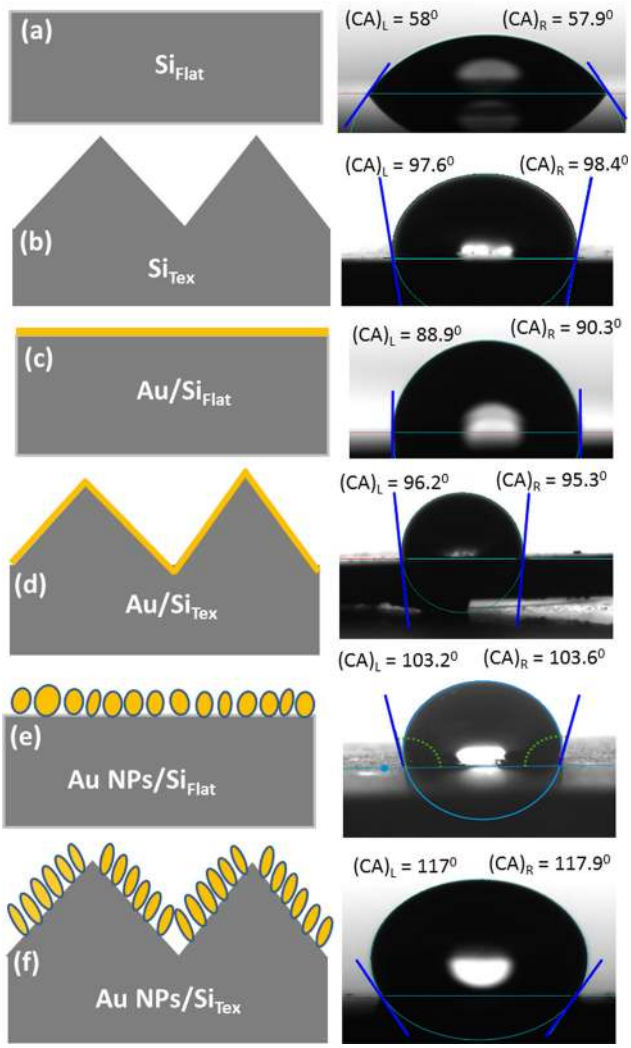

FIG. 4. Schematic representation (left panel) and the corresponding result (right panel) of the CA measurements for (a) flat and (b) textured Si surfaces, whereas conformal Au films on (c) flat and (d) textured Si surfaces. The formation of Au NPs by annealing at 400 °C on (e) flat and (f) textured Si surfaces (dual-scale structure). The left and right side CAs are indicated by $(CA)_L$ and $(CA)_R$, respectively.

Si_{Tex} at RT [see Fig. 4(d) and adjacent panel]. Although there is no significant change in the average CA with and without Au film on Si_{Tex}, a close inspection of the shape of water droplet in the former looks more spherical than on bare Si facets. The reason is two-fold: (i) low surface energy of Au (stated above)[16] and (ii) positive chemical potential of the pyramid apex[24] that drives the water droplet towards the slanted Si facets. However, The CA increases further from 89° ± 1° to 103° ± 1° on Si_{Flat} by annealing at 400 °C [shown in right panel of Fig. 4(e)] due to the formation of Au NPs. On the other hand, annealed-mediated evolution of Au NPs on Si pyramids gives a CA of 118° ± 1° [see right panel of Fig. 4(f)].

Since the increase in CA depends on the solid-liquid contact area, both aerial density and height of the microstructures would be the deciding factors for choosing the Wenzel and Cassie-Baxter models.[4] However, the shape of water droplet on Si_{Tex} [Fig. 4(b)] is most likely associated with the dominant role of weight of water droplet over contact forces with higher surface roughness, and so can wet the valleys of

the faceted structures as the one documented earlier in Ref. 45. Hence, this result can be explained only by the Wenzel's model rather than Cassie-Baxter.[46] In fact, the increase in CA up to ~118° in Au NP-decorated Si pyramids [Fig. 4(f)] can further be attributed to the involvement of dual rough surfaces as in case of lotus leaf.[47] According to the Wenzel's model, the hydrophobic effect can be defined by $\cos\theta^* = r\cos\theta$, where θ^* is the measured CA on a rough surface, θ is the average CA on the corresponding flat surface, and r is the fractional surface area representing the ratio between the actual area and projected area. In fact, the cosine of CA more than 90° gives negative value, and thus it is not straightforward to calculate the roughness for closed packed Si pyramids (with nonuniform size, shape, and distribution).[3] This requires detailed study of the CA hysteresis and corresponding theory, which are now under investigation and will be reported elsewhere.

Being good light scattering centers, focus is now to understand the role of Au NPs in controlling specular reflectance (R) when grown on Si pyramids. In order to understand the underlying mechanism, UV-VIS experiments have been carried out in a systematic way in the range of 300–800 nm (Fig. 5). As can be seen, R in the order of 40%–50% in the near-infrared (NIR) region for polished Si_{Flat} surfaces (spectrum in gray) is reduced drastically below 0.4% after chemical texturing (highlighted in black), in good agreement with the previous report.[12] Close inspection, however, reflects a gradual increase in R from ~0.3 to 1.4% when moving from visible to UV region; but it can be suppressed below 0.5% in the UV region in the presence of conformal Au film (spectrum in green). Following the growth of Au NPs at 400 °C, average R is found to drop further down to ~0.4% below the wavelength of 500 nm, though it intensifies slowly in the NIR region (blue spectrum).

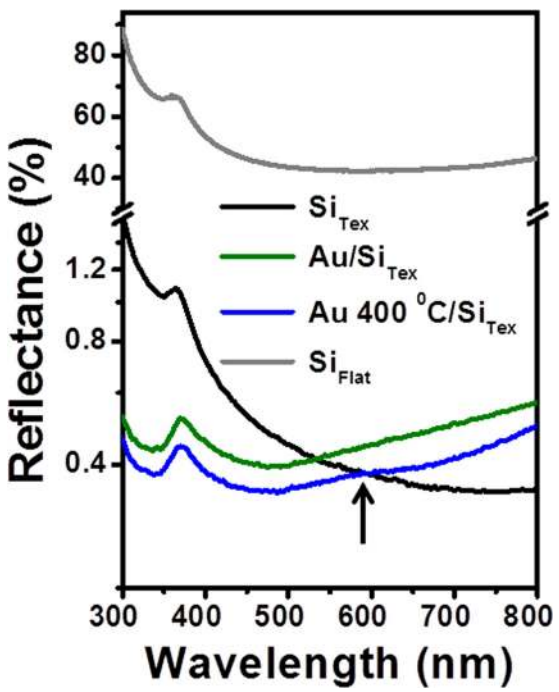

FIG. 5. Specular reflectance of flat Si (gray) and textured Si (black), while for Au films on textured Si before (olive) and after (blue) annealing at 400 °C.

Given the reflection of a white light from the graded refractive index at the air/Si interface, the observed low R from Si_{Tex} surfaces above 500 nm can be discussed in the framework of multiple scattering of light from Si facets.[48] This leads to the enhancement of absorption up to a factor of $4n^2$, where n is the refractive index of Si.[48] On the other hand, the increase in R below 500 nm can be explained in the light of limitation of geometrical optics effect.[49] On the other side, sudden reduction of R by depositing Au films is most likely due to the cancelation of the air-side scattered light from both the Au layer and underlying Si substrate by destructive interference, when the incident light bounces between adjacent pyramids before final escape, as suggested earlier in the presence of NPs.[22] It seems that the reduction of R in the presence of self-ordered Au NPs at the pyramid edges can also be associated with the enhanced coupling between the forward scattered light from Au NPs with the underlying Si because of having pitches below 300 nm [inset of Fig. 1(d)] with respect to the spectral range.[21,22] The small NPs dispersed on Si facets can also participate in reducing R as suggested earlier in Ref. 50. Moreover, the appearance of a weak and broad hump in the wavelength of ~500–650 nm (indicated by an upward arrow) can be attributed to the air-side scattering loss from Au NPs with dimension in the order of 100 nm and above.[51]

IV. CONCLUSIONS

In conclusion, we report annealing temperature dependent growth of Au NPs on Si facets, especially self-ordering at the edges of Si pyramids at 400 °C with improved hydrophobicity. The detailed XRD analyses confirmed the formation of Au nanocrystals at 400 °C, though Au and Si atoms did not mix at the Au/Si interfaces as established from TEM investigations. The CA was however increased to ~118° in the presence of Au NPs on Si pyramids, and discussed it in the light of Wenzel's model. Such dual-scale structure was found to be suitable for suppressing visible range specular reflectance, especially in the UV region due to the combined effect of graded refractive index in the uncovered regions of Si facets and the coupling of scattered light from Au NPs with the Si underneath. Finally, the observed control over hydrophobicity along with improving optical absorption in Au NP-decorated Si pyramids will be a benchmark for developing multifunctional devices ranging from biomedical to optoelectronics applications.

ACKNOWLEDGMENTS

The authors would like to thank Dr. P. K. Sahoo and Dr. S. Chatterjee from NISER and CSIR-IMMT Bhubaneswar for their kind help in SEM and contact angle measurements, respectively. One of the authors A.K. would like to acknowledge scientific visit and research support received from the Institute of Physics Bhubaneswar, and also the financial support from Alexander von Humboldt Foundation for purchasing contact angle measurement system.

[1]D. P. Singh and J. P. Singh, Appl. Phys. A **114**, 1189 (2014).
[2]V. A. Ganesh, H. K. Raut, A. S. Nair, and S. Ramakrishna, J. Mater. Chem. **21**, 16304 (2011).
[3]T. Koishi, K. Yasuoka, S. Fujikawa, T. Ebisuzaki, and X. C. Zeng, Proc. Natl. Acad. Sci. U.S.A. **106**, 8435 (2009).

[4]B. Bhushan and Y. C. Jung, Nanotechnology **17**, 2758 (2006).
[5]Y. Y. Yan, N. Gao, and W. Barthlott, Adv. Colloid Interface Sci. **169**, 80 (2011).
[6]X. Wang, B. Ding, J. Yu, and M. Wang, Nano Today **6**, 510 (2011).
[7]W. Barthlott and C. Neinhuis, Planta **202**, 1 (1997); C. Neinhuis and W. Barthlott, Ann. Bot. **79**, 667 (1997).
[8]K. Y. Lai, Y. R. Lin, H. P. Wang, and J. H. He, CrystEngComm **13**, 1014 (2011).
[9]B. Xu and Z. Cai, Appl. Surf. Sci. **254**, 5899 (2008).
[10]Y. H. Xiu, L. B. Zhu, D. W. Hess, and C. P. Wong, Nano Lett. **7**, 3388 (2007).
[11]Y. Xiu, S. Zhang, V. Yelundur, A. Rohatgi, D. W. Hess, and C. P. Wong, Langmuir **24**, 10421 (2008).
[12]C. P. Saini, A. Barman, M. Kumar, P. K. Sahoo, T. Som, and A. Kanjilal, Appl. Phys. Lett. **105**, 123901 (2014).
[13]D. Qi, N. Lu, H. Xu, B. Yang, C. Huang, M. Xu, L. Gao, Z. Wang, and L. Chi, Langmuir **25**, 7769 (2009).
[14]S. Pazokifard, S. Farrokhpay, M. Mirabedini, and M. Esfandeh, Prog. Org. Coat. **87**, 36 (2015).
[15]W. Zhao, L. Wang, and Q. Xue, J. Phys. Chem. C **114**, 11509 (2010).
[16]S. Meng, E. G. Wang, and S. W. Gao, J. Chem. Phys. **119**, 7617 (2003).
[17]M. R. Rasch, E. Rossinyol, J. L. Hueso, B. W. Goodfellow, J. Arbiol, and B. A. Korgel, Nano Lett. **10**, 3733 (2010).
[18]P. A. Lewis, H. Ahmed, and T. Sato, J. Vac. Sci. Technol. B **16**, 2938 (1998).
[19]S. Mekhilef, R. Saidur, and M. Kamalisarvestani, Renewable Sustainable Energy Rev. **16**, 2920 (2012).
[20]S. A. Jang, H. J. Lee, C. V. Thompson, C. A. Ross, and Y. J. Oh, APL Mater. **3**, 126103 (2015).
[21]P. Spinelli, M. Hebbink, R. de Waele, L. Black, F. Lenzmann, and A. Polman, Nano Lett. **11**, 1760 (2011).
[22]K. X. Wang, Z. Yu, S. Sandhu, V. Liu, and S. Fan, Optica **1**, 388 (2014).
[23]N. Li, P. Zhao, and D. Astruc, Angew. Chem. Int. Ed. **53**, 1756 (2014).
[24]A. L. Giermann and C. V. Thompson, Appl. Phys. Lett. **86**, 121903 (2005).
[25]J. C. Hulteen, J. Mater. Chem. **7**, 1075 (1997).
[26]J. Zheng, Z. Zhu, H. Chen, and Z. Liu, Langmuir **16**, 4409 (2000).
[27]S. Mohapatra, Y. K. Mishra, D. K. Avasthi, D. Kabiraj, J. Ghatak, and S. Varma, Appl. Phys. Lett. **92**, 103105 (2008).
[28]K. Govatsi, A. Chrissanthopoulos, V. Dracopoulos, and S. N. Yannopoulos, Nanotechnology **25**, 215601 (2014).
[29]P. Farzinpour, A. Sundar, K. D. Gilroy, Z. E. Eskin, R. A. Hughes, and S. Neretina, Nanotechnology **23**, 495604 (2012).
[30]A. Rota, A. Martinez-Gil, G. Agnus, E. Moyen, T. Maroutian, B. Bartenlian, R. Mégy, M. Hanbücken, and P. Beauvillain, Surf. Sci. **600**, 1207 (2006).
[31]I. Martin-Bragado, Appl. Phys. Lett. **98**, 233109 (2011); I. Martin-Bragado and B. Sklenard, J. Appl. Phys. **112**, 024327 (2012).
[32]W. Ostwald, Z. Phys. Chem. (Leipzig) **34**, 495 (1900).
[33]G. H. Stout and L. H. Jensen, *X-Ray Structure Determination: A Practical Guide* (Macmillan, New York, 1968).
[34]B. D. Cullity, *Elements of X Ray Diffraction* (Addison-Wesley Publishing Comp. Inc., Massachusetts, 1956).
[35]M. Birkholz, *Thin Film Analysis by X-Ray Scattering* (John Wiley & Sons, 2006).
[36]M. Eberlein, S. Escoubas, M. Gailhanou, O. Thomas, J.-S. Micha, P. Rohr, and R. Coppard, Phys. Status Solidi A **204**, 2542 (2007).
[37]K. C. Nguyen, Adv. Nat. Sci: Nanosci. Nanotechnol. **3**, 045008 (2012).
[38]J. Slezák, M. Ondřejček, Z. Chvoj, V. Cháb, H. Conrad, S. Heun, Th. Schmidt, B. Ressel, and K. C. Prince, Phys. Rev. B **61**, 16121 (2000).
[39]F. Banhart, *In-Situ Electron Microscopy at High Resolution* (World Scientific, 2008).
[40]Y. C. Liu and T. C. Chuang, J. Phys. Chem. B **107**, 12383 (2003).
[41]A. Kanjilal, S. Gemming, L. Rebohle, A. Muecklich, T. Gemming, M. Voelskow, W. Skorupa, and M. Helm, Phys. Rev. B **83**, 113302 (2011).
[42]G. S. Chen, C. B. Boothroyd, and C. J. Humphreys, Appl. Phys. Lett. **62**, 1949 (1993).
[43]C. C. Ahn and O. L. Krivanek, *EELS Atlas: A Reference Collection of Electron Energy Loss Spectra Covering All Stable Elements* (Gatan, Warrendale, 1983).
[44]J. K. Bal, S. Kundu, and S. Hazra, Mater. Chem. Phys. **134**, 549 (2012).
[45]X. Li, B. K. Tay, P. Miele, A. Brioude, and D. Cornu, Appl. Surf. Sci. **255**, 7147 (2009).
[46]Q. S. Zheng, Y. Yu, and Z. H. Zhao, Langmuir **21**, 12207 (2005).
[47]M. Nosonovsky and B. Bharat, Microelectron. Eng. **84**, 382 (2007).
[48]P. Spinelli, M. A. Verschuuren, and A. Polman, Nat. Commun. **3**, 692 (2012).
[49]R. B. Stephens and G. D. Cody, Thin Solid Films **45**, 19 (1977).
[50]S. Das, A. Kundu, H. Saha, and S. Datta, Plasmonics **10**, 1895 (2015).
[51]S. H. Lim, W. Mar, P. Matheu, D. Derkacs, and E. T. Yu, J. Appl. Phys. **101**, 104309 (2007).